



ZnO/BiOI heterojunction photoanodes with enhanced photoelectrochemical water oxidation activity

Mingyue Wang^{a,1}, Andreas Kafizas^{b,c,2}, Sanjayan Sathasivam^{a,d,3}, Matthew O. Blunt^a, Benjamin Moss^b, Soranyel Gonzalez-Carrero^b, Claire J. Carmalt^{a,*,4}

^a Department of Chemistry, University College London, 20 Gordon Street, London WC1H 0AJ, UK

^b Department of Chemistry, Molecular Science Research Hub, Imperial College London, London W12 0BZ, UK

^c Grantham Institute for Climate Change and the Environment and London Centre for Nanotechnology, Imperial College London, London SW7 2AZ, UK

^d School of Engineering, London South Bank University, London SE1 0AA, UK

ARTICLE INFO

Keywords:

BiOI
ZnO
Heterojunction
Water oxidation
Aerosol-assisted chemical vapour deposition (AACVD)

ABSTRACT

ZnO/BiOI heterojunction photoanode thin films were prepared by aerosol-assisted chemical vapour deposition, and the impact of growth temperature and film thickness on the water oxidation functionality was systematically investigated. A top ZnO layer with a thickness of 120 nm (deposited at 350 °C) and a 390 nm thick BiOI layer (deposited at 300 °C) were found to achieve the best photoelectrochemical performance of the heterojunction. The ZnO/BiOI heterojunction exhibited a significant increase in photoelectrochemical activity, with a photocurrent of 0.27 mA·cm⁻² observed at 1.1 V_{RHE} (350 nm, 2.58 mW·cm⁻²), which is ~ 2.2 times higher than that of single-layer ZnO and far higher than that of BiOI. Photoluminescence spectroscopy and transient absorption spectroscopy measurements showed that there was effective charge transfer across the heterojunction which spatially separated charge carriers and increased their lifetime and ability to drive photoelectrochemical water oxidation.

1. Introduction

To mitigate against the climate change there is a pressing need to move away from fossil fuel based energy sources such as natural gas, oil and coal. One of the most promising ways of achieving this is through photoelectrochemical (PEC) water splitting to produce hydrogen fuel and oxygen [1]. This process was demonstrated by Fujishima and Honda in 1972, where a TiO₂ photoanode was used to drive the oxidation of water [2]. Although TiO₂ remains the most popular and heavily studied material in this field, its wide optical band gap (≥ 3.0 eV) limits the amount of light that can be harvested from the solar spectrum to ~4% [3]. Therefore, various studies have been implemented in the search for semiconductors with high activity across the visible wavelengths of the solar spectrum for PEC water splitting. Bismuth oxyhalides, BiOX (where X = Cl, Br and I), have received attention due to their visible light activated photocatalytic properties.

The tetragonal crystal structure of BiOX is composed of [Bi₂O₂]²⁺ layers sandwiched between double X⁻ slabs [4]. This layered structure of BiOX generates internal electric fields, which is thought to assist the separation of charge carriers and minimize carrier recombination that is detrimental to PEC efficiency [5]. Of the three oxyhalides, BiOI has the narrowest band gap (1.8 – 1.9 eV) and shows promising activity for PEC water oxidation under visible light irradiation [6–8]. Furthermore, the indirect BiOI band gap also helps keep photogenerated charges separate thus reducing recombinative losses [9]. To date, thin film BiOI have been prepared via electrochemical deposition [10], chemical vapour transport [11], spray pyrolysis deposition [12] and aerosol-assisted chemical vapour deposition (AACVD) [7]. Interestingly, BiOI with n-type or p-type behavior is possible depending on the synthetic route. For example, Zhang et al. reported p-type BiOI via low temperature chemical bath methods whereas Mullins et al. were able to synthesise nanoplatelet BiOI thin films with n-type characteristics [12,13].

* Corresponding author.

E-mail address: c.j.carmalt@ucl.ac.uk (C.J. Carmalt).

¹ ORCID: 0000-0003-3084-7619

² ORCID: 0000-0002-2282-4639

³ ORCID: 0000-0002-5206-9558

⁴ ORCID: 0000-0003-1788-6971

To increase the photocatalytic and PEC performance of BiOI further, diverse approaches have been employed. For instance, doping of BiOI with metal elements, such as Fe, Zn and In, to form favorable crystal defects that can positively impact photocatalytic activity [14–16]. However, one of the most promising approaches for enhancing activity is to build a heterojunction with secondary materials [17]. Through coupling two semiconductors with the appropriate band energies, charge carrier separation can be promoted, increasing carrier lifetimes and thus enabling ability to drive kinetically challenging reactions like water oxidation [10,18,19]. Numerous BiOI-based heterojunctions have been investigated by combining BiOI with different materials, such as TiO_2 [20], ZnO [14,22] and BiVO_4 [21]. These heterojunctions all showed improved activities in various photocatalytic applications, such as PEC water splitting [10,21–24].

ZnO is a widely investigated material in PEC water splitting with non-toxicity, relatively high electron mobility and chemical stability [25]. ZnO can be easily grown on the surface of other semiconductor materials with a range of morphologies using various methods and at low cost [26]. ZnO is a suitable heterojunction partner for BiOI as it has a band gap of 3.37 eV allowing it to be activated by UV light whilst letting the visible wavelengths pass through to the BiOI [27]. It can also help move charge carriers away from the ZnO to the BiOI layer where its intrinsic layered nature and associated electric fields help reduce charge carrier recombination [13,17].

Most research about the heterojunction of ZnO and BiOI has been focused on the photocatalytic performance of the heterojunction for the degradation of organic pollutants [13,24,28–30], but the study of PEC water splitting, and detailed characterizations have been rarely reported [24]. In addition, the preparation methods are limited, with hydro-/solvothermal synthesis being the most common. Some of the methods require further steps to deposit powder samples into films for photocatalytic applications, and for some methods it is difficult to achieve scale-up production necessary for industrialization. In this work, heterojunctions containing n-type ZnO and n-type BiOI were grown for the first time using AACVD, which is an adaptable, scalable and inexpensive method for thin-film deposition. BiOI/ZnO (i.e. BiOI at the top and ZnO at the bottom) and ZnO/BiOI (i.e. ZnO at the top and BiOI at the bottom) heterojunctions were deposited on FTO, and their PEC activities and stability as photoanodes were investigated. The physical and functional properties of the BiOI/ZnO and ZnO/BiOI heterojunctions and parent materials were characterized. No obvious improvement in activity was seen in the BiOI/ZnO heterojunction when compared with the parent materials. However, the ZnO/BiOI heterojunction showed a significantly improved PEC performance, which was measured using a range of techniques, such as current-voltage curves, incident-photon-to-current efficiency (IPCE) and applied bias photo-to-current efficiency (ABPE). Transient absorption spectroscopy (TAS) was utilized for the first time, to our knowledge, to study the charge carrier behaviour of the ZnO/BiOI heterojunction, which indicated effective charge transfer across the heterojunction, resulting in approximately double the population of charge carriers in the ZnO and BiOI layers of the heterojunction (at the resolution of our measurement; $\sim 10 \mu\text{s}$) compared to the individual parent materials. In an effort to optimize the activity of the ZnO/BiOI system, the influence of deposition temperature and thickness of the top ZnO layer was also systematically studied.

2. Experimental section

2.1. Film fabrication

2.1.1. BiOI thin film

BiOI thin films were deposited following a literature procedure [7]. BiI_3 (0.5897 g, 1 mmol) in anhydrous dimethylformamide (25 mL) was stirred for 30 mins to form the precursor solution. Compressed air (flow rate: 1.0 L/min) was used as the carrier gas. BiOI films were grown on FTO glass (NSG TEC 15) substrate (15 cm \times 4.5 cm) at 300 °C. The

duration of the deposition was 60 min. Films were allowed to cool naturally to room temperature.

2.1.2. ZnO thin film via AACVD

2.28 mmol (0.5 g) Zinc acetate dihydrate ($\text{Zn}(\text{OAc})_2 \cdot 2 \text{H}_2\text{O}$) was dissolved in methanol (25 mL), and the precursor solution was stirred for 20 mins. The carrier gas was compressed air (flow rate: 1.0 L/min). ZnO was grown on FTO substrates (NSG TEC 15) at 350 °C for 25 mins. Substrates were cooled naturally to room temperature.

For the BiOI/ZnO heterojunction, the ZnO film was deposited on the FTO substrate followed by the BiOI film. For the ZnO/BiOI heterojunction, the BiOI film was deposited on the FTO substrate. Then, as well as 350 °C, the ZnO film was deposited on top of the BiOI film at 300, 400 and 450 °C. The obtained heterojunctions will be referred to as ZnO-300 °C /BiOI, ZnO-350 °C /BiOI, ZnO-400 °C /BiOI and ZnO-450 °C /BiOI. In addition to 2.28 mmol $\text{Zn}(\text{OAc})_2 \cdot 2 \text{H}_2\text{O}$, precursor solutions with 0.46 mmol (0.1 g), 1.37 mmol (0.3 g), 3.19 mmol (0.7 g) and 4.10 mmol (0.9 g) $\text{Zn}(\text{OAc})_2 \cdot 2 \text{H}_2\text{O}$ were used in the film deposition at 350 °C to obtain ZnO films with various thickness. The obtained heterojunctions will be referred to as ZnO-0.46/BiOI, ZnO-1.37/BiOI, ZnO-2.28/BiOI, ZnO-3.19/BiOI and ZnO-4.10/BiOI.

2.2. Physical characterisation

Grazing-incident X-ray diffraction (GIXRD) patterns were measured from 5° to 60° (0.05° steps and 0.5 s/step) using a Panalytical Empyrean diffractometer. The X-ray source was $\text{Cu K}\alpha$ ($\lambda = 1.5406 \text{ \AA}$) at 40 kV with 40 mA emission current. The angle of the incident beam was 1°. A JEOL JSM-7600 field emission scanning electron microscope (SEM) was used to study the film morphologies. A Shimadzu UV-2700 spectrometer was used to measure UV-Vis-NIR spectra in transmission mode between 300 and 1000 nm wavelength range. X-ray photoelectron spectroscopy (XPS) was undertaken on a Thermo Scientific K-alpha spectrometer (monochromated $\text{Al K}\alpha_1$ radiation (8.3418 eV)). A dual beam system was employed for charge compensation. Survey scans (0–1200 eV) at 50 eV pass energy. Depth profiling XPS using an Ar^+ ion beam to etch the surface. All peak positions were calibrated to adventitious carbon (284.8 eV). XPS data was processed using CasaXPS®. Photoluminescence (PL) spectra were obtained at room temperature using a Horiba Fluorolog Fluorometer. Surface roughness was measured using atomic force microscopy Keysight 5500 scanning probe atomic force microscope (AFM). Images were collected in tapping mode using Si cantilevers with a resonant frequency of $\sim 70 \text{ kHz}$ and a $\sim 2 \text{ N m}^{-1}$ spring constant (NuNano SCOUT-70). Images were taken over a projected area of 5 $\mu\text{m} \times 5 \mu\text{m}$. The roughness factor was determined by dividing the measured surface area by the projected area. TAS was measured in air over a microsecond-second timescale in transmission mode. The excitation source was a Nd:YAG laser (OPOTEK Opolette 355 II, $\sim 6 \text{ ns}$ pulse width) generating 355 nm UV light from the third harmonic ($\sim 0.60 \text{ mJ cm}^{-2}$ per pulse, with a pulse rate of 0.5 Hz). Samples were excited from the top side. 100 W Benthall IL1 quartz halogen lamp was used to generate the probe light. Long pass filters (Comar Instruments) between the lamp and sample were necessary to reduce sample irradiation from short wavelengths. Transient changes in transmission through the sample was collected by a lens (2" diameter, 2" focal length), sent to a monochromator (Oriel Cornerstone 130) and measured at select wavelengths between 550 and 1100 nm. Time-resolved changes in transmission were detected using a Si photodiode (Hamamatsu S3071) and converted to absorption. Data at times faster than 3.6 ms was recorded using an oscilloscope (Tektronics DPO3012) after passing through an amplifier box (Costronics). Data at times slower than 3.6 ms was recorded on a National Instrument DAQ card (NI USB-6251). Each kinetic trace was obtained from the average of 200 laser pulses. A photodiode (Thorlabs DET10A) from a laser scatter triggered the acquisitions. A home built Labview software was used to acquire and process the data.

2.3. Photoelectrochemical testing and calculations

PEC experiments were carried out in a three-electrode configuration with a quartz window (0.5 cm²). A Na₂SO₄ aqueous solution (0.5 M) at a pH of 6.6. The as-fabricated film, Ag/AgCl/saturated-KCl (Metrohm) and Pt mesh were used as the working electrode, reference electrode and counter electrode, respectively. Both the JV curves and IPCE measurements were taken with an ozone-free xenon lamp (75 W, Hamamatsu) coupled with a monochromator (OBB-2001, Photon Technology International). An optical power meter (PM 100, Thorlabs) and a power sensor (S120UV, Thorlabs) were used to measure the light intensity. An Autolab potentiostat (PGSTAT12 with an FRA2 module) was implemented to apply voltages and measure current flows.

The applied voltage in our current-voltage curves were reported against the reversible hydrogen electrode (V_{RHE}), converted by the Nernst equation:

$$V_{RHE} = V_{Ag/AgCl} + 0.05916\text{pH} + V_{Ag/AgCl}^{\ominus} \quad (1)$$

where $V_{Ag/AgCl}$ is the applied potential *versus* the Ag/AgCl reference electrode, pH is the electrolyte pH and $V_{Ag/AgCl}^{\ominus}$ is the standard reference potential (0.197 V_{NHE} at 25 °C). The IPCE was calculated as follows:

$$\text{IPCE}(\%) = (I_{ph} \times 1239.8) / (P_{mono} \times \lambda) \times 100 \quad (2)$$

where I_{ph} (mA·cm⁻²) is the photocurrent, P_{mono} (mW·cm⁻²) is the power, and λ (nm) is the wavelength of the monochromated light. And the theoretical solar photocurrent (TSP) was calculated by multiplying the IPCE with the AM 1.5 solar spectrum, then converting this into the photocurrent [31]:

$$\text{TSP}(\text{mAcm}^{-2}) = \int_{400\text{nm}}^{280\text{nm}} \text{IPCE} \times \text{AM1.5}(\text{m}^{-2} \cdot \text{s}^{-1} \cdot \text{nm}^{-1}) \times 1000 / (1C \times 10000) \quad (3)$$

where 1 C is 6.241×10^{18} electron.

ABPE of ZnO, BiOI and ZnO/BiOI was calculated from the equation [32]:

$$\text{ABPE}(\%) = J \times (1.23 V_{RHE} - V_{app}) / P_{light} \times 100.$$

Where J is the photocurrent density, V_{app} is the applied voltage vs. RHE, and P_{light} is the power density of 1 sun illumination (100 mW·cm⁻²).

3. Results and discussion

3.1. Crystal structure and film composition

In this work, to improve the PEC performance of the BiOI film, heterojunctions with ZnO, including BiOI/ZnO and ZnO/BiOI, were grown via AACVD. Highly transparent ZnO films were obtained from the AACVD of Zn(OAc)₂·2 H₂O in methanol under compressed air flow at temperatures ranging from 300 to 450 °C. Orange coloured BiOI films were obtained from the AACVD of BiI₃ in DMF under compressed air flow at 300 °C. Both BiOI/ZnO and ZnO/BiOI heterojunctions were deposited from separate depositions of each layer, as described above. The BiOI/ZnO and ZnO/BiOI heterojunctions were both orange in appearance. The performance of ZnO/BiOI heterojunctions were studied further and optimized to determine the impact of deposition temperature and ZnO layer thickness on PEC performance.

The composition and crystallographic structure of the deposited ZnO and BiOI films were determined by GIXRD (Fig. 1). Only peaks for hexagonal ZnO and tetragonal BiOI were visible for both single layer films on FTO. From Fig. 1, it can be seen that the BiOI films display preferential growth in the (102) and (110) planes, consistent with n-type BiOI films grown by spray pyrolysis [12]. It has been reported that, compared with the (001) plane, the exposed (110) facets of BiOI possess better oxygen adsorption capacity and charge transfer efficiency, which

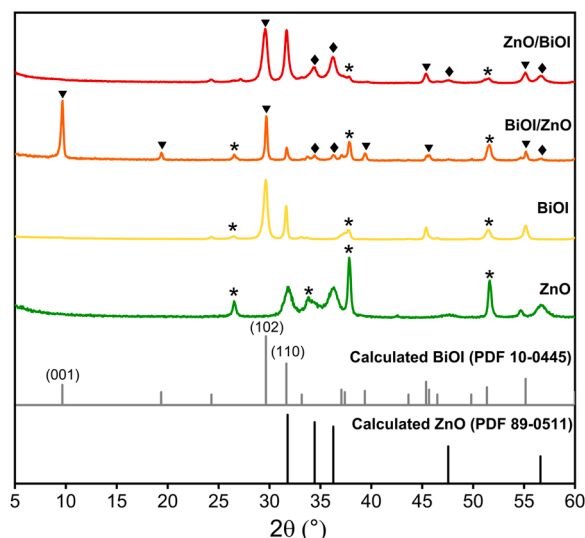


Fig. 1. GIXRD patterns of ZnO, BiOI, BiOI/ZnO and ZnO/BiOI films deposited on FTO, where all ZnO films were grown from Zn(OAc)₂·2 H₂O (2.28 mmol) at 350 °C. The asterisk, square and triangle peaks indicate positions of reflections from FTO, ZnO and BiOI respectively.

is beneficial to photocatalysis [33,34]. In addition, the charge extraction could be improved through the connection of the BiOI layer with (110) preferential orientation and the ZnO film, as the in-plane direction of BiOI has higher charge carrier mobilities [8,35]. In the bilayer heterojunctions, only peaks from the ZnO and BiOI phases described above were visible in the GIXRD patterns. Unit cell parameters and average crystallite size of deposited films (Table 1) were determined from the GIXRD data. Unit cell parameters obtained from single-layer films and heterojunctions were very similar, indicating that there was little to no ion diffusion between the layers in both BiOI/ZnO and ZnO/BiOI heterojunctions. It is possible that the relatively low deposition temperature (300 or 350 °C) in the AACVD process helped minimize interlayer ion diffusion. In addition, the average crystallite size of ZnO and BiOI in the ZnO/BiOI heterojunction, calculated from the Scherrer equation, were similar to those from both single layers.

In order to find the heterojunction with optimized performance, a variety of ZnO films of different thickness and properties were deposited on the BiOI films (to form ZnO/BiOI heterojunctions) by changing the growth parameters in the AACVD process. With an increase of deposition temperatures from 300 °C to 400 °C, peaks corresponding to ZnO grew narrower and with increased intensity, demonstrating improved

Table 1

Unit cell parameters (a, c) cell volume (V) and average crystallite size of ZnO, BiOI, BiOI/ZnO and ZnO/BiOI films, where all ZnO films deposited from Zn(OAc)₂·2 H₂O (2.28 mmol) at 350 °C.

Films	a [Å]	c [Å]	V [Å ³]	Average crystallite size (Å)
ZnO standard	3.249	5.205	47.6	-
BiOI standard	3.994	9.149	145.9	-
ZnO	3.248	5.205 (7)	47.56 (7)	139 (4)
BiOI	3.996	9.148 (8)	146.10	178 (4)
BiOI/ZnO	3.251	5.191	47.51 (17)	231 (4)
	(6)	(13)	(11)	
	3.995	9.149 (3)	146.03	214 (4)
	(2)	(11)		
ZnO/BiOI	3.251	5.199 (7)	47.58 (9)	159 (4)
	(3)	(15)	(25)	
	3.997	9.148	146.14	163 (9)
	(1)	(15)	(25)	

crystallinity in the ZnO films (Fig. S1a). However, at 450 °C, the bottom BiOI film started to decompose to β -Bi₂O₃ (Fig. S1a), which is consistent with the reported thermal stability of BiOI [23]. In addition, ZnO films with various thickness were obtained through controlling the amount of precursor transferred in the AACVD reaction. The relative peak intensity between the BiOI and ZnO phases indicated a gradual increase in thickness of the top ZnO layer as the amount of precursor transferred was increased (Fig. S1b).

The surface composition of the BiOI/ZnO and ZnO/BiOI heterojunctions (Fig. 2) were studied using high resolution XPS. In addition, the single-layer parent materials of BiOI and ZnO (Fig. S2) were also studied, with peak positions comparable to previous reports observed [20,24,36]. For the BiOI/ZnO heterojunction, the Bi 4f spectra was best fitted using a pair of doublets. The primary component matched to Bi³⁺ (Bi 4f_{7/2} = 158.8 eV) in BiOI and the secondary component matched to Bi metal (Bi 4f_{7/2} = 157.3 eV). The minor metallic component observed is believed to be due to the instability of BiOI under incident X-rays during analysis leading to photoreduction and has previously been observed for many Bi based XPS studies [7,13]. The I 3d signal produced a 3d_{5/2} peak centred at 618.5 eV therefore corresponding to I⁻ [13]. For the ZnO/BiOI film, a Zn doublet was observed with the Zn 2p_{3/2} centred at 1021.0 eV corresponding to Zn²⁺ [24,36]. All peak positions were consistent with those seen for the single layer parent films (Fig. S2a-c). Due possibly to pinholes and cracks on the top layer, Zn was detected on the BiOI/ZnO films and some Bi and I were detected for the ZnO/BiOI films (Fig. S2d-f). XPS depth profiling was carried out on the ZnO/BiOI heterojunction to show the Bi:Zn ratio increased with increasing etch time and depth of analysis (Fig. S3).

3.2. Morphological characterization

Fig. 3 provides the top-down SEM images. The ZnO film featured tightly packed rounded crystals (200 – 300 nm in diameter) slightly protruded from the substrate, which is common for AACVD-ZnO films [37]. The BiOI film was composed of uniform square nanoplatelets with edge sizes of 500 – 900 nm, with previous studies of BiOI films on FTO showing similar structures [7,11,12]. Compared with the calculated average crystallite size (Table 1), the larger particle size observed in the SEM images indicated that nanoparticles in both ZnO and BiOI films were composed of multiple crystallites. The BiOI/ZnO heterojunction showed a similar surface morphology to the BiOI film (Fig. 3c). For the ZnO/BiOI heterojunction, the top ZnO layer displayed a significantly different morphology from the single layer ZnO film, with the particles growing into larger rods and less densely packed (Fig. 3e). In the ZnO/BiOI heterojunction, the ZnO layer grew along the nanoplatelet edge of the bottom BiOI film, leading to the formation of rod-shaped particles. This growth trend could be further detailed by imaging the series of ZnO/BiOI heterojunctions with different ZnO film thickness

(Fig. 4). With the increase of ZnO film thickness, the film morphology became closer to that of single-layer ZnO grown on top of FTO. In addition, the deposition temperature of ZnO also had an effect on the film morphology (Fig. S4). A higher growth temperature resulted in a rougher rod surface of the ZnO formed. Due to the thermal decomposition of BiOI into Bi₂O₃, particles of ZnO-450 °C/BiOI were aggregated, and no ZnO particles were observed (Fig. S4c), which is consistent with the GIXRD patterns (Fig. S1a). For both heterojunctions, the double-layer structure could be seen clearly through the cross-sectional SEM (Fig. 3d, f). These indicated that the BiOI/ZnO and ZnO/BiOI films (ZnO deposited from 2.28 mmol Zn(OAc)₂·2 H₂O at 350 °C) had film thickness of ca 0.300 nm/100 nm and ca. 120 nm/390 nm, respectively. Furthermore, for the series of ZnO/BiOI heterojunctions formed with increasing amount of Zn precursor (from 0.46 mmol to 4.10 mmol), the thickness variation of the top ZnO film was seen clearly in cross-sectional SEM images, increasing from 20 nm to 260 nm, respectively (Fig. S5).

3.3. Optical properties and band gap analysis

The optical properties of the single-layer films, ZnO and BiOI, and the BiOI/ZnO and ZnO/BiOI heterojunctions (ZnO deposited from 2.28 mmol Zn(OAc)₂·2 H₂O at 350 °C) were investigated using UV-visible spectroscopy (Fig. 5a). The single-layer ZnO film had a high degree of visible light transmission, with a sharp band edge at around 375 nm. The wide band gap, and thus poor solar harvesting, is one of the major drawbacks that hinders the activity of ZnO in solar-driven water splitting applications. In contrast, the single-layer BiOI film displayed a band edge at 650 nm. The transmittance spectrum of ZnO/BiOI is similar to that of BiOI, with a minor blue shift of the band edge. This shows that the ZnO/BiOI heterojunction has a wide absorption range from UV to yellow visible light, and thus, has significantly greater solar harvesting than ZnO alone. However, in addition to the band edge at around 620 nm, an extra band edge at 375 nm from ZnO was observed in the transmittance spectrum of BiOI/ZnO due to the incomplete coverage of the BiOI film. The Tauc method was used to calculate the optical band gaps of ZnO and BiOI (Fig. 5b, c) [38], showing that the direct band gap of the ZnO was ~3.32 eV, while the BiOI film had an indirect band gap of ~1.79 eV; both correspond with reported values in the literature [7,11,37]. The influence of deposition temperature and thickness of the top ZnO layer on the optical properties of the ZnO/BiOI heterojunctions were also studied. For heterojunctions with different ZnO deposition temperatures, an obvious blue shift of the band edge was seen due to the decomposition of BiOI at high temperatures, coinciding with a film colour change from orange to pale yellow (Fig. S6a). A slight variation of the transmission was observed with the increase of ZnO film thickness, with the band edge showing no significant change within the range of experimental error (Fig. S6b).

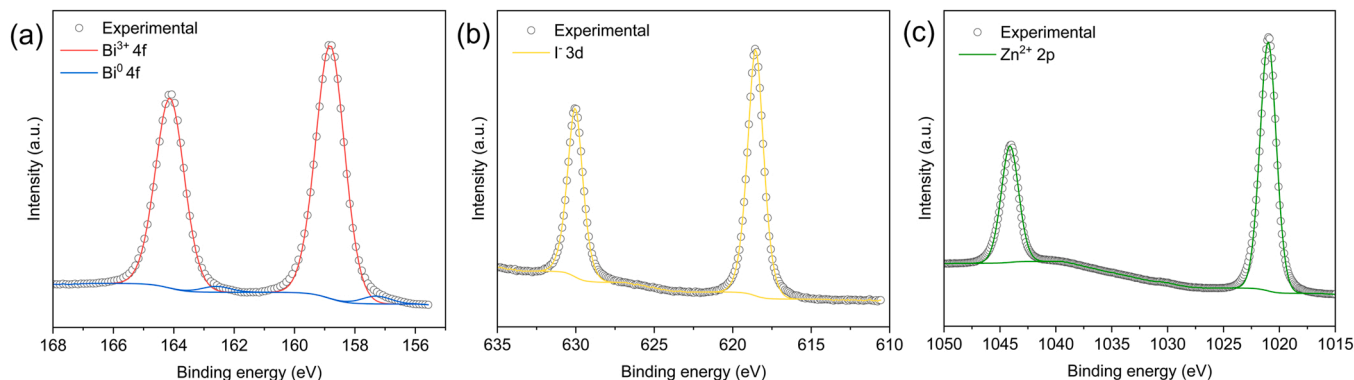


Fig. 2. High resolution XPS spectra of (a) Bi 4f, (b) I 3d from the BiOI/ZnO and (c) Zn 2p from the ZnO/BiOI heterojunction films grown via AACVD, where all ZnO films were deposited from 2.28 mmol Zn(OAc)₂·2 H₂O at 350 °C.

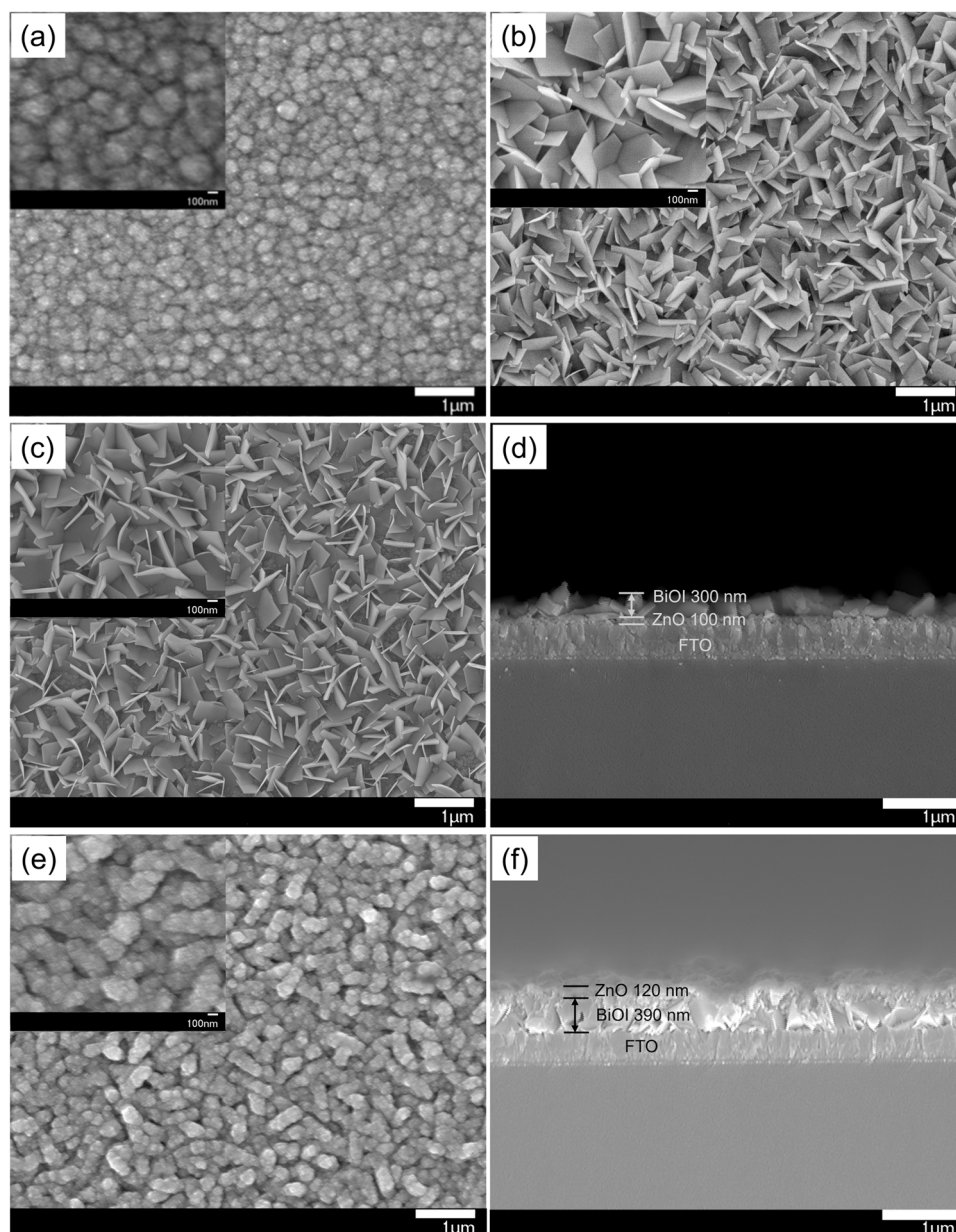


Fig. 3. Top-down SEM images of (a) ZnO, (b) BiOI, (c) BiOI/ZnO and (e) ZnO/BiOI; cross-sectional SEM images of (d) BiOI/ZnO and (f) ZnO/BiOI, where all ZnO films were grown from 2.28 mmol $\text{Zn}(\text{OAc})_2 \cdot 2 \text{H}_2\text{O}$ at 350 °C.

3.4. PEC measurements

The conductivity type of BiOI is prone to be influenced by the fabrication method. It has been reported that n-type BiOI is obtained for films deposited via AACVD [7]. In current-voltage curves, the anodic photocurrent observed in the as-prepared BiOI films herein is also indicative of n-type conductivity. Aiming to investigate the activity of the ZnO/BiOI heterojunction for PEC water oxidation, films were first examined using current-voltage measurements in 0.5 M Na_2SO_4 solution (Fig. 6a). Sweeping the voltage from 0.13 V_{RHE} to 1.61 V_{RHE} , current-voltage curves were obtained under light illumination (350 nm, $2.58 \text{ mW}\cdot\text{cm}^{-2}$) and in the dark. Under irradiation, the photocatalytic current of the single-layer BiOI film was negligible compared with the single-layer ZnO film and the ZnO/BiOI heterojunction. The onset potentials for PEC water oxidation of ZnO and ZnO/BiOI were similar ($\sim 0.3 V_{\text{RHE}}$), while BiOI existed an onset potential of $\sim 0.6 V_{\text{RHE}}$. The photocurrent of the ZnO film reached a plateau at $\sim 0.1 \text{ mA}\cdot\text{cm}^{-2}$, from

0.6 V_{RHE} . Whereas the current-voltage curve of the ZnO/BiOI heterojunction kept increasing in the tested voltage range and exhibited a photocurrent of $0.27 \text{ mA}\cdot\text{cm}^{-2}$ at 1.1 V_{RHE} . This value is almost 3 times higher than that of ZnO. It was shown that compared with both single layer materials, the PEC performance was improved significantly due to the construction of the ZnO/BiOI heterojunction. Interestingly, the other heterojunction with an inverse structure, BiOI/ZnO, showed an extremely low PEC activity (Fig. S7). Compared with the single-layer BiOI film, the PEC activity of the BiOI/ZnO heterojunction was only marginally enhanced, and substantially worse than that of the single-layer ZnO film. The poor coverage of the top BiOI layer, shown in GIXRD, SEM and XPS characterizations, might reduce the light harvesting of BiOI/ZnO. In addition, it has been reported that in PEC testing, a layer of bismuth hydroxide may form on the BiOI film surface exposed to aqueous solutions, acting as an insulating layer inhibiting charge transfer [12]. All of these could lead to the low PEC activity of the BiOI/ZnO structure.

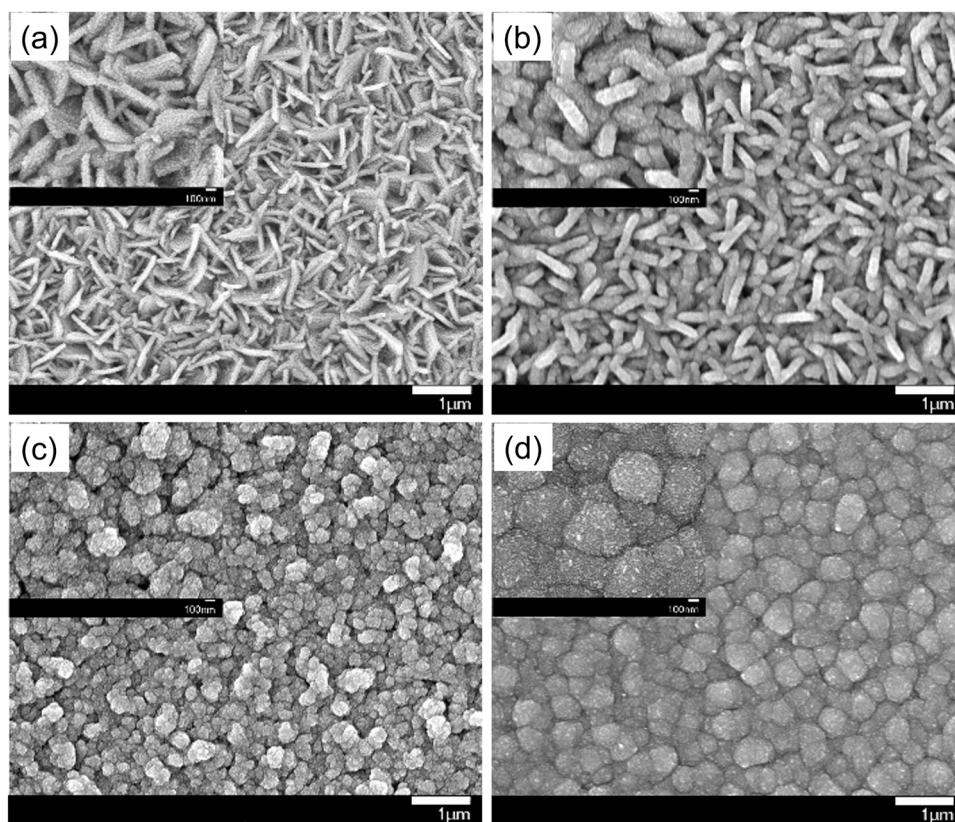


Fig. 4. Top-down SEM images of ZnO/BiOI films with ZnO grown from (a) 0.46, (b) 1.37, (c) 3.19 and (d) 4.10 mmol $\text{Zn}(\text{OAc})_2 \cdot 2 \text{H}_2\text{O}$ at 350 °C.

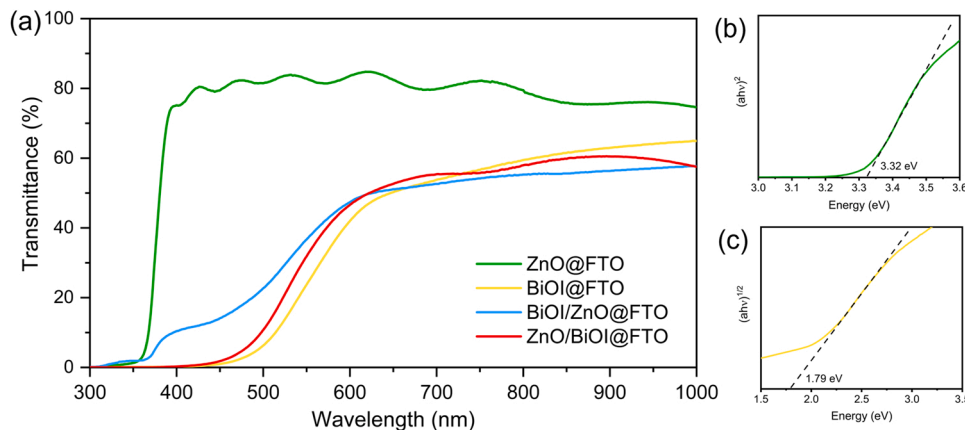


Fig. 5. (a) Transmittance spectra of ZnO, BiOI, and ZnO/BiOI films deposited on FTO. Optical bandgaps were determined *via* the Tauc plot (a plot of $(\alpha h\nu)^n$ vs. photon energy), for (b) ZnO, where $n = 2$ for the direct allowed bandgap transition and (c) BiOI, where $n = 1/2$ for the indirect allowed bandgap transition.

Therefore, the enhanced PEC properties of the ZnO/BiOI heterojunction was investigated in more detail. The impact of the deposition temperature and thickness of the top ZnO film on the photocatalytic water oxidation function was studied. A significant improvement of the photocurrent for ZnO grown at 350 °C compared with 300 °C was attributed to the increased crystallinity of the ZnO film (Fig. S1a, S8a). When films are deposited at low temperatures, a low degree of crystallinity, which is unfavorable to the PEC performance, is typically exhibited [39]. Conversely, at temperatures of 400 °C and above, the BiOI film underneath started to decompose, and the PEC performance of the heterojunction dropped dramatically. For ZnO/BiOI heterojunctions with different ZnO film thickness, the photocurrent of the heterojunction increased gradually with the thicker ZnO films. For film

thickness > 120 nm, a reduction of the PEC performance was observed (Fig. S8b). The photocurrent depends on the number of photogenerated charge carriers from semiconductors. Initial increase of the ZnO film thickness could benefit the absorption of incident light in UV range [40], leading to the production of more charge carriers. However, further increase of the film thickness is likely to inhibit the transfer of charges formed in the bulk of ZnO (or the BiOI layer) to the surface of ZnO where water oxidation takes place, resulting in a decrease in photocurrent.

ABPE is helpful to quantify the photo-response efficiency of photoelectrodes under an applied potential. The ABPE (%) of ZnO and BiOI, and the ZnO/BiOI heterojunction was plotted against applied potential vs. RHE (Fig. S9). The highest ABPE of ZnO is 0.18% at 0.68 V_{RHE} , while the ABPE of BiOI is negligible (0.0036% at 0.97 V_{RHE}). ZnO/BiOI

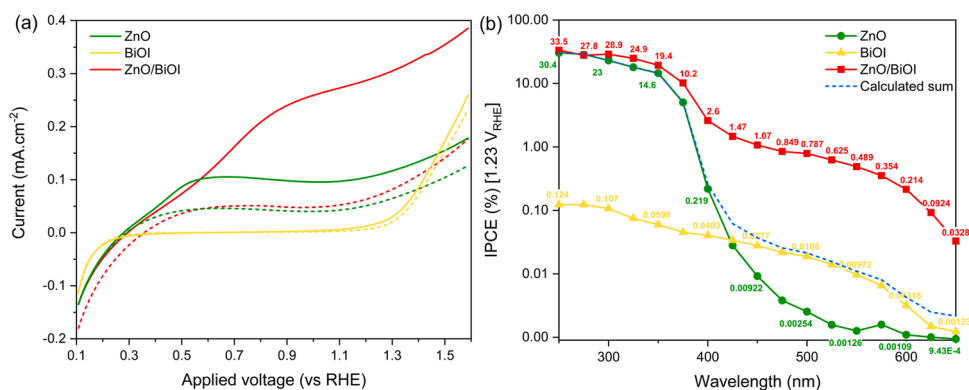


Fig. 6. (a) Current–voltage curves of ZnO, BiOI, and ZnO/BiOI were measured with front-side illumination (350 nm, 2.58 mW·cm⁻²) (solid lines) and in the dark (dashed lines). The voltage was swept from 0.13 V_{RHE} to 1.61 V_{RHE} at a rate of 10 mV·s⁻¹. (b) IPCE for ZnO, BiOI, and ZnO/BiOI photoanodes. All ZnO films were grown from 2.28 mmol Zn(OAc)₂·2 H₂O at 350 °C.

reached the maximum efficiency of 0.33% at 0.87 V_{RHE}, which is almost 2x and 100x higher than that of ZnO and BiOI respectively.

IPCE was measured for single-layer ZnO and BiOI, and the ZnO/BiOI heterojunction over the 250–650 nm wavelength range, holding the photoanode at 1.23 V_{RHE} (Fig. 6b). Samples were irradiated from the front. The IPCE of ZnO/BiOI was larger than both ZnO and BiOI over the whole wavelength range, showing a quantum efficiency of ~10 to ~33% in UV region and ~0.1 to ~3% in the visible region. Furthermore, the IPCE of ZnO/BiOI was also higher than the calculated sum IPCE of ZnO and BiOI, which is attributed to the synergetic effect of forming a heterojunction; reducing electron-hole recombination through the enhanced spatial separation of charges.

In order to predict the performance of samples in practical solar water splitting applications, TSP was calculated through multiplying IPCE with the AM 1.5 solar spectrum (Fig. 7) [41]. The TSPs of BiOI, ZnO and the ZnO/BiOI heterojunction were ~0.0028 mA·cm⁻², ~0.12 mA·cm⁻² and ~0.27 mA·cm⁻² respectively. Compared with both single-layer samples, the TSP of the ZnO/BiOI heterojunction was significantly greater than the sum of its parent materials (more than double this value), again showing the improved performance of the heterojunction. Due to the smaller bandgap of BiOI, the light harvesting limitation of ZnO in the visible range was overcome by forming the ZnO/BiOI heterojunction. The more than double enhancement in solar activity determined for the ZnO/BiOI heterojunction is primarily because the solar spectrum is composed of substantially more visible light (44%) than UV light (4%). A table comparing the performance of ZnO, BiOI and ZnO/BiOI photoelectrodes with similar structures or fabricated with similar film deposition methods was prepared (Table S1). The ZnO/BiOI heterojunction produced herein showed a higher performance than previous work.

As determined by AFM, the roughness factors of the ZnO, BiOI and ZnO/BiOI films were ~1.04, ~1.76 and ~1.14, respectively (Fig. 8).

Although nanostructuring and increasing surface roughness can increase PEC activity, the roughest BiOI film showed the lowest PEC activity, and although ZnO and ZnO/BiOI had similar surface roughness, the ZnO/BiOI sample was more than twice as active as the ZnO sample. This showed that surface area is not an influence factor on the PEC performance of these films.

The recombination rate of photogenerated electrons and holes was assessed via PL spectroscopy. A stronger PL peak can be attributed to a higher rate of recombination. Under 400 nm excitation, the BiOI film showed two significant peaks at 441 and 548 nm (Fig. 9). The peak at 441 nm could be attributed to the direct band gap recombination of charge carriers [42], while the formation of the other peak likely resulted from the existence of vacancies [12,43]. Under the same excitation condition, the steady-state PL signal was significantly lower in the ZnO/BiOI heterojunction, showing a similar emission spectrum to the ZnO parent material. This indicated charge transfer occurred from the BiOI layer to the ZnO layer in the heterojunction, reducing electron-hole recombination and quenching the PL signal. This supported the notion that the heterojunction improves charge carrier separation and therefore synergistically improves PEC activity.

The charge carrier dynamics in the ZnO/BiOI films, and its parent materials, were investigated using TAS [3]. The transient absorption decay kinetics are shown in Fig. S10. In the parent ZnO material, near zero signals were seen in the blue region of the electromagnetic spectrum, but long-lived bleach signals were observed in the red (Fig. S10a). Bleach signals arise when there is a loss in ground state absorption [44]. These bleach signals were weak (up to ~-0.01 mΔO.D.) and decayed to half of the original signal measured at 10 μs (t_{50%}) in ~200 ms. These findings were similar to previous studies of ZnO thin films [45]. In the parent BiOI material, stronger transient absorption was seen in the blue (up to ~0.13 mΔO.D.) than in the red (up to ~0.02 mΔO.D.) (Fig. S10b). Unlike the parent ZnO, no bleach signals were seen in BiOI. In the parent

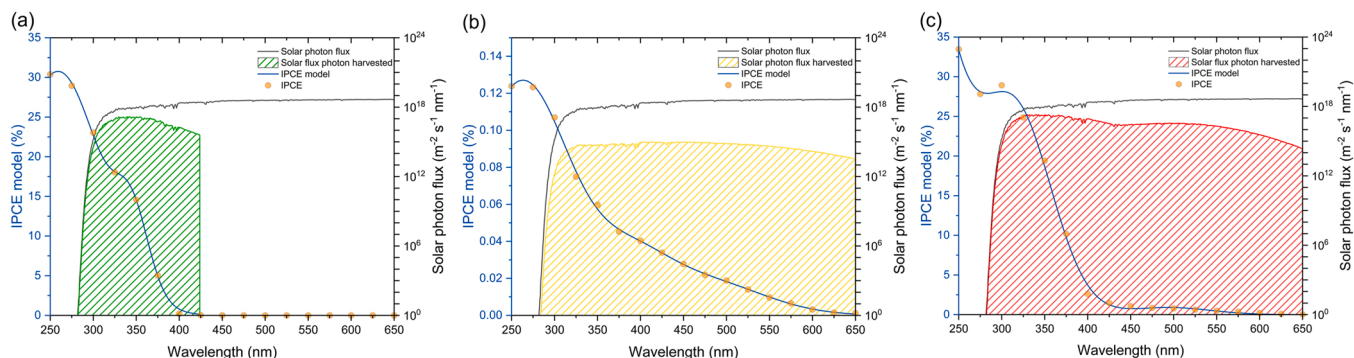


Fig. 7. TSPs of (a) ZnO, (b) BiOI and (c) ZnO/BiOI when held at 1.23 V_{RHE}. All ZnO films were grown from 2.28 mmol Zn(OAc)₂·2 H₂O at 350 °C.

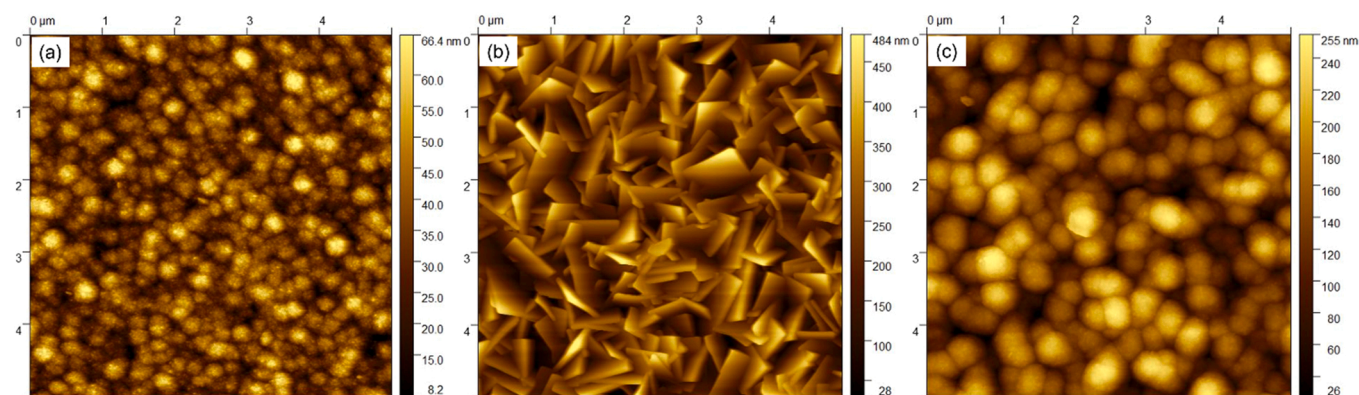


Fig. 8. AFM images of (a) ZnO, (b) BiOI and (c) ZnO/BiOI films. All ZnO films were grown from 2.28 mmol $\text{Zn}(\text{OAc})_2 \cdot 2 \text{H}_2\text{O}$ at 350 °C. All images were of a $5 \times 5 \mu\text{m}$ square area.

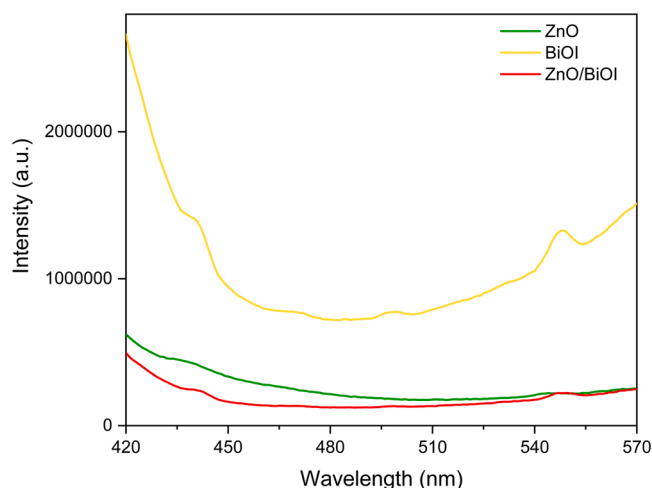


Fig. 9. Photoluminescence spectra of ZnO, BiOI, and ZnO/BiOI excited at 400 nm. All ZnO films were grown from 2.28 mmol $\text{Zn}(\text{OAc})_2 \cdot 2 \text{H}_2\text{O}$ at 350 °C.

BiOI, signals decayed with power law behavior, which was indicative of trap-mediated recombination [46]. These signals decayed with a $t_{50\%}$ of $\sim 60 \mu\text{s}$. There are few long timescale transient absorption studies of BiOI in the literature, with most focusing on the ultrafast timescale (fs to ns) [47–49]. Nevertheless, slow timescale studies were carried out by Pu et al. who studied p-type BiOI photocathodes in operando and observed bleach signals across the visible region, which were most strong in the

blue and decayed with a $t_{50\%}$ of $\sim 20 \mu\text{s}$ [50]. Also, Zhang et al. saw much faster decays in BiOI powders in solution, with a $t_{50\%}$ of $\sim 0.5 \mu\text{s}$ [51]. In our ZnO/BiOI heterojunction, hybrid behavior, somewhere between that of the parent materials, was observed (Fig. S10c). A strong absorption was observed in the blue (up to $\sim 0.12 \text{ m}\Delta\text{O.D.}$), similar to the BiOI parent material, which decayed at a similar rate ($t_{50\%} \sim 40 \mu\text{s}$). However, in the red, long-lived bleach signals were observed ($t_{50\%} \sim 300 \text{ ms}$), similar to the ZnO parent material. The transient absorption spectra for the ZnO/BiOI heterojunction and parent materials are provided in Fig. S11. As discussed briefly above, the ZnO parent material shows a broad yet weak bleach signal across the visible, with this being most intense at $\sim 900 \text{ nm}$ (Fig. S11a). In the BiOI parent material, a strong and positive transient absorption signal was observed in the blue, which was weaker in the red (Fig. S11b). And in the ZnO/BiOI heterojunction, a composite spectrum of its parent materials was observed at early timescales ($\sim 10 \mu\text{s}$); however, by $\sim 10 \text{ ms}$, the transient absorption spectrum had completely bleached (Fig. S11c).

The transient absorption decays at the probe wavelengths of 550 and 1100 nm are compared in Fig. 10. It should be noted, that according to UV–visible transmission measurements (Fig. 5a), approximately half of the pump excitation used in our transient absorption measurements was absorbed by the ZnO layer and all of the pump excitation was absorbed by the BiOI layer. This meant that an equivalent amount of light was absorbed in the ZnO layer of the heterojunction and parent material and approximately half of the light was absorbed in the BiOI layer of the heterojunction compared with the parent material. At a probe wavelength of 550 nm, similarly strong transient absorption was observed at early timescales ($\sim 10 \mu\text{s}$) in the ZnO/BiO heterojunction and the BiOI parent material (Fig. 10a). This was despite the fact that only

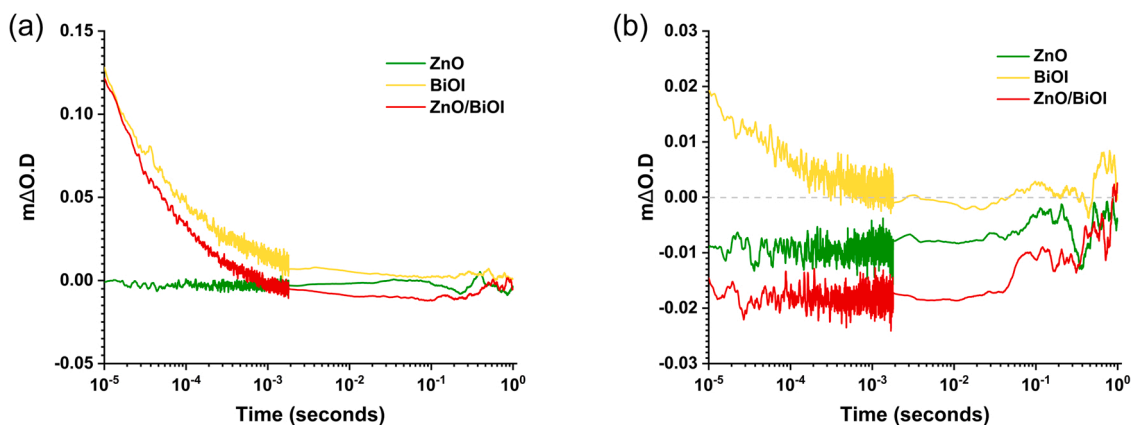


Fig. 10. Transient absorption decay kinetics for ZnO, BiOI, and ZnO/BiOI measured at the probe wavelengths (a) 550 nm and (b) 1100 nm from $10 \mu\text{s}$ after the laser pulse until 1 s ($\lambda_{\text{exc}} = 355 \text{ nm}$, $\sim 6 \text{ ns}$ pulse width, $\sim 0.60 \text{ mJ}\cdot\text{cm}^{-2}$, 0.5 Hz).

approximately half of the pump light likely reached the BiOI layer in the heterojunction as compared with the parent BiOI material. And at a probe wavelength of 1100 nm, almost twice the bleach signal was seen at early timescales in the ZnO/BiOI heterojunction compared with the ZnO parent material (Fig. 10b). Overall, these findings showed that early timescale charge carrier populations in the ZnO/BiOI heterojunction - accounting for differences in pump absorption - were approximately twice the expected amounts as compared to the parent materials. This showed that the heterojunction was effective in separating charge. Nevertheless, the kinetics of charge carrier recombination in the respective layers of the ZnO/BiOI heterojunction were similar to the parent materials.

The stability of ZnO, BiOI and ZnO/BiOI was tested at 1.23 V_{RHE} for 1.5-hour duration (Fig. S12). The photocurrent of BiOI dropped significantly in the first 100 s, which is consistent with the poor stability of reported BiOI films due to photocorrosion [7,12]. ZnO and ZnO/BiOI showed similar stability and exhibited a rapid decay in photocurrent in 700 s. There was a 90% and 85% decrease after a period of 1.5 h for ZnO and ZnO/BiOI respectively. Current-voltage curves were measured pre- and post- 1.5-hour stability testing (Fig. S13). Consistent with the stability test, significant decrease of the photocurrent was observed for the heterojunction and parent materials. Under 1 sun irradiation, the photocurrent at 1.23 V_{RHE} decreased from 0.390 mA·cm⁻² to 0.165 mA·cm⁻², from 0.035 mA·cm⁻² to 0.026 mA·cm⁻², and from 1.441 mA·cm⁻² to 0.723 mA·cm⁻² for ZnO, BiOI and the ZnO/BiOI respectively. GIXRD patterns were collected for the heterojunction and its parental materials after the stability test to study the compositional variation (Fig. S14). In Fig. S14a, the intensity of peaks from ZnO relative to that of FTO substrate decreased after the stability test, showing the dissolution of ZnO. According to two possible corrosion reactions of ZnO [52]:



Only soluble Zn ions could be produced. Therefore, no extra peaks from decomposition appeared in GIXRD patterns. For the BiOI film, no significant change was observed before and after the stability test (Fig. S14b). This result is consistent with the reported study that upon the exposure to water, an insulating layer of bismuth hydroxide might be formed only on the surface, which would inhibit the charge transfer and could not be observed in XRD [12]. Because of aforementioned reasons, in the ZnO/BiOI heterojunction, the relative intensity of peaks from ZnO decreased while there was no obvious change of peaks from BiOI (Fig. S14c). The Faradaic efficiency of the ZnO/BiOI heterojunction towards PEC water oxidation was attempted (Fig. S15). However, the relatively rapid photocorrosion of ZnO made it challenging to measure O₂ evolution that corresponded to PEC water oxidation alone (reaction 2). A similar behavior was also seen in the ZnO parent material (Fig. S16). In the future, a passivation layer or surface co-catalysts could be employed to help protect the ZnO/BiOI heterojunction from photocorrosion, achieving more long-term PEC stability in aqueous electrolytes required for a commercial device.

4. Conclusions

In conclusion, thin films of ZnO, BiOI and their heterojunctions, BiOI/ZnO and ZnO/BiOI were successfully fabricated via AACVD, a versatile, inexpensive and scalable technique. The composition and clear double layer structure of the constituted heterojunctions were identified by GIXRD, XPS and SEM imaging. While the BiOI/ZnO structure was far less active towards PEC water oxidation, the ZnO/BiOI heterojunction showed a remarkable enhancement in activity compared with its parent materials. The ZnO/BiOI heterojunction, with the 120 nm thick ZnO film grown at 350 °C, exhibited the best PEC performance through studying the influence of the ZnO film thickness and deposition

temperature. From IPCE measurements at 1.23 V_{RHE}, the theoretical solar photocurrent for the ZnO/BiOI heterojunction was 0.271 mA·cm⁻², which was ~100 and ~2.2 times higher than that of the BiOI (0.0028 mA·cm⁻²) and ZnO (0.121 mA·cm⁻²) parent materials, respectively. UV-visible spectroscopy, PL and first-reported TAS studies showed that the synergetic improvements in PEC performance found in the ZnO/BiOI heterojunction could be attributed to increased visible-light activity of the heterojunction and enhanced charge carrier separation between the BiOI and ZnO layers. Herein, we developed a scalable synthetic route to a heterojunction photoanode that shows substantially higher performance than its parent materials. In the future, this strategy may prove to be a viable route to the large-scale production of high performance photoanodes for use in commercial water splitting devices.

CRediT authorship contribution statement

Mingyue Wang: Conceptualization, Methodology, Investigation, Writing – original draft. **Andreas Kafizas:** Investigation, Writing – review & editing, Resources. **Sanjayan Sathasivam:** Investigation, Writing – review & editing. **Matthew O. Blunt:** Investigation. **Benjamin Moss:** Investigation, Writing – review & editing. **Soranyel Gonzalez-Carrero:** Investigation. **Claire J. Carmalt:** Supervision, Writing – review & editing, Conceptualization.

Declaration of Competing Interest

The authors declare that they have no known competing financial interests or personal relationships that could have appeared to influence the work reported in this paper.

Data Availability

No data was used for the research described in the article.

Acknowledgments

M.W. thanks University College London and China Scholarship Council for the joint Ph.D. scholarship. A.K. thanks the EPSRC for a Capital Award Emphasizing Support for Early Career Researchers (EP/S017852/1) and the Royal Society for an Equipment grant (RSG\R1\180434).

Appendix A. Supporting information

Supplementary data associated with this article can be found in the online version at doi:10.1016/j.apcatb.2023.122657.

References

- [1] B. Moss, O. Babacan, A. Kafizas, A. Hankin, A review of inorganic photoelectrode developments and reactor scale-up challenges for solar hydrogen production, *Adv. Energy Mater.* 11 (2021), 2003286, <https://doi.org/10.1002/aenm.202003286>.
- [2] A. Fujishima, K. Honda, Electrochemical photolysis of water at a semiconductor electrode, *Nature* 238 (1972) 37–38, <https://doi.org/10.1038/238037a0>.
- [3] A. Kafizas, R. Godin, J.R. Durrant, Charge carrier dynamics in metal oxide photoelectrodes for water oxidation, in: *Semiconductors and Semimetals*, Elsevier, 2017, pp. 3–46, <https://doi.org/10.1016/bs.semsem.2017.02.002>.
- [4] F.A. Bannister, The crystal-structure of the bismuth oxyhalides, *Mineral. Mag. J. Mineral. Soc.* 24 (1935) 49–58, <https://doi.org/10.1180/minmag.1935.024.149.01>.
- [5] Y. Mi, M. Zhou, L. Wen, H. Zhao, Y. Lei, A highly efficient visible-light driven photocatalyst: two dimensional square-like bismuth oxyiodine nanosheets, *Dalton Trans.* 43 (2014) 9549–9556, <https://doi.org/10.1039/c4dt00798k>.
- [6] H. An, Y. Du, T. Wang, C. Wang, W. Hao, J. Zhang, Photocatalytic properties of BiOX (X = Cl, Br, and I, *Rare Met.* 27 (2008) 243–250, [https://doi.org/10.1016/S1001-0521\(08\)60123-0](https://doi.org/10.1016/S1001-0521(08)60123-0).
- [7] D.S. Bhachu, S.J.A. Moniz, S. Sathasivam, D.O. Scanlon, A. Walsh, S.M. Bawaked, M. Mokhtar, A.Y. Obaid, I.P. Parkin, J. Tang, C.J. Carmalt, Bismuth oxyhalides: synthesis, structure and photoelectrochemical activity, *Chem. Sci.* 7 (2016) 4832–4841, <https://doi.org/10.1039/C6SC00389C>.

- [8] V. Andrei, R.A. Jagt, M. Rahaman, L. Lari, V.K. Lazarov, J.L. MacManus-Driscoll, R. L.Z. Hoye, E. Reisner, Long-term solar water and CO₂ splitting with photoelectrochemical BiOI-BiVO₄ tandems, *Nat. Mater.* 21 (2022) 864–868, <https://doi.org/10.1038/s41563-022-01262-w>.
- [9] K.L. Zhang, C.M. Liu, F.Q. Huang, C. Zheng, W.D. Wang, Study of the electronic structure and photocatalytic activity of the BiOCl photocatalyst, *Appl. Catal. B.* 68 (2006) 125–129, <https://doi.org/10.1016/j.apcatb.2006.08.002>.
- [10] X. Zhang, H. Yang, B. Zhang, Y. Shen, M. Wang, BiOI-TiO₂ nanocomposites for photoelectrochemical water splitting, *Adv. Mater. Interfaces* 3 (2016), <https://doi.org/10.1002/admi.201500273>.
- [11] L. Ye, J. Chen, L. Tian, J. Liu, T. Peng, K. Deng, L. Zan, BiOI thin film via chemical vapor transport: photocatalytic activity, durability, selectivity and mechanism, *Appl. Catal. B.* 130–131 (2013) 1–7, <https://doi.org/10.1016/j.apcatb.2012.10.011>.
- [12] N.T. Hahn, S. Hoang, J.L. Self, C.B. Mullins, Spray pyrolysis deposition and photoelectrochemical properties of n-type BiOI nanoplatelet thin films, *ACS Nano* 6 (2012) 7712–7722, <https://doi.org/10.1021/nn3031063>.
- [13] J. Jiang, X. Zhang, P. Sun, L. Zhang, ZnO/BiOI heterostructures: photoinduced charge-transfer property and enhanced visible-light photocatalytic activity, *J. Phys. Chem. C.* 115 (2011) 20555–20564, <https://doi.org/10.1021/jp205925z>.
- [14] H. Li, Z. Yang, J. Zhang, Y. Huang, H. Ji, Y. Tong, Indium doped BiOI nanosheets: preparation, characterization and photocatalytic degradation activity, *Appl. Surf. Sci.* 423 (2017) 1188–1197, <https://doi.org/10.1016/j.apsusc.2017.06.301>.
- [15] N. Talreja, S. Afreen, M. Ashfaq, D. Chauhan, A.C. Mera, C.A. Rodríguez, R. v Mangalajaya, Bimetal (Fe/Zn) doped BiOI photocatalyst: an effective photodegradation of tetracycline and bacteria, *Chemosphere* 280 (2021), 130803, <https://doi.org/10.1016/j.chemosphere.2021.130803>.
- [16] N. Talreja, M. Ashfaq, D. Chauhan, A.C. Mera, C.A. Rodríguez, Strategic doping approach of the Fe-BiOI microstructure: an improved photodegradation efficiency of tetracycline, *ACS Omega* 6 (2021) 1575–1583, <https://doi.org/10.1021/acsomega.0c05398>.
- [17] S. Li, W. Xu, L. Meng, W. Tian, L. Li, Recent progress on semiconductor heterojunction-based photoanodes for photoelectrochemical water splitting, *Small Sci.* (2022), 2100112, <https://doi.org/10.1002/smss.202100112>.
- [18] Z. Wang, M. Chen, D. Huang, G. Zeng, P. Xu, C. Zhou, C. Lai, H. Wang, M. Cheng, W. Wang, Multiply structural optimized strategies for bismuth oxyhalide photocatalysis and their environmental application, *Chem. Eng. J.* 374 (2019) 1025–1045, <https://doi.org/10.1016/j.cej.2019.06.018>.
- [19] S. Selim, L. Francàs, M. García-Tecedor, S. Corby, C. Blackman, S. Gimenez, J. R. Durrant, A. Kafizas, WO₃/BiVO₄: Impact of charge separation at the timescale of water oxidation, *Chem. Sci.* 10 (2019) 2643–2652, <https://doi.org/10.1039/c8sc04679d>.
- [20] L. Cai, J. Yao, J. Li, Y. Zhang, Y. Wei, Sonochemical synthesis of BiOI-TiO₂ heterojunction with enhanced visible-light-driven photocatalytic activity, *J. Alloy. Compd.* 783 (2019) 300–309, <https://doi.org/10.1016/j.jallcom.2018.12.387>.
- [21] K.-H. Ye, Z. Chai, J. Gu, X. Yu, C. Zhao, Y. Zhang, W. Mai, BiOI-BiVO₄ 4 photoanodes with significantly improved solar water splitting capability: p-n junction to expand solar adsorption range and facilitate charge carrier dynamics, *Nano Energy* 18 (2015) 222–231, <https://doi.org/10.1016/j.nanoen.2015.10.018>.
- [22] H. Wang, Y. Liang, L. Liu, J. Hu, P. Wu, W. Cui, Enriched photoelectrocatalytic degradation and photoelectric performance of BiOI photoelectrode by coupling rGO, *Appl. Catal. B.* 208 (2017) 22–34, <https://doi.org/10.1016/j.apcatb.2017.02.055>.
- [23] C. Chang, H.C. Yang, N. Gao, S.Y. Lu, Core/shell p-BiOI/n-β-Bi₂O₃ heterojunction array with significantly enhanced photoelectrochemical water splitting efficiency, *J. Alloy. Compd.* 738 (2018) 138–144, <https://doi.org/10.1016/j.jallcom.2017.12.145>.
- [24] P.-Y. Kuang, J.-R. Ran, Z.-Q. Liu, H.-J. Wang, N. Li, Y.-Z. Su, Y.-G. Jin, S.-Z. Qiao, Enhanced photoelectrocatalytic activity of BiOI nanoplatelet-zinc oxide nanorod p-n heterojunction, *Chem. A Eur. J.* 21 (2015) 15360–15368, <https://doi.org/10.1002/chem.201501183>.
- [25] J. Kegel, I.M. Povey, M.E. Pemble, Zinc oxide for solar water splitting: a brief review of the material's challenges and associated opportunities, *Nano Energy* 54 (2018) 409–428, <https://doi.org/10.1016/j.nanoen.2018.10.043>.
- [26] J. Kegel, I.M. Povey, M.E. Pemble, Zinc oxide for solar water splitting: a brief review of the material's challenges and associated opportunities, *Nano Energy* 54 (2018) 409–428, <https://doi.org/10.1016/j.nanoen.2018.10.043>.
- [27] M. Ma, Y. Huang, J. Liu, K. Liu, Z. Wang, C. Zhao, S. Qu, Z. Wang, Engineering the photoelectrochemical behaviors of ZnO for efficient solar water splitting, *J. Semicond.* 41 (2020), 091702, <https://doi.org/10.1088/1674-4926/41/9/091702>.
- [28] J. Liu, S. Zou, B. Lou, C. Chen, L. Xiao, J. Fan, Interfacial electronic interaction induced engineering of ZnO-BiOI heterostructures for efficient visible-light photocatalysis, *Inorg. Chem.* 58 (2019) 8525–8532, <https://doi.org/10.1021/acs.inorgchem.9b00834>.
- [29] J. Tang, Y. Xue, C. Ma, S. Zhang, Q. Li, Facile preparation of BiOI/T-ZnOw p-n heterojunction photocatalysts with enhanced removal efficiency for rhodamine B and oxytetracycline, *N. J. Chem.* 46 (2022) 13010–13020, <https://doi.org/10.1039/D2NJ01609E>.
- [30] P. Zeng, H. Yu, M. Chen, W. Xiao, Y. Li, H. Liu, J. Luo, J. Peng, D. Shao, Z. Zhou, Z. Luo, Y. Wang, B. Chang, X. Wang, Flower-like ZnO modified with BiOI nanoparticles as adsorption/catalytic bifunctional hosts for lithium-sulfur batteries, *J. Energy Chem.* 51 (2020) 21–29, <https://doi.org/10.1016/j.jecchem.2020.03.040>.
- [31] F. Pinto, A. Wilson, B. Moss, A. Kafizas, Systematic exploration of WO₃/TiO₂ 2 heterojunction phase space for applications in photoelectrochemical water splitting, *J. Phys. Chem. C.* 2022 (2022) 884, <https://doi.org/10.1021/acs.jpcc.1c08403>.
- [32] T. Hisatomi, J. Kubota, K. Domen, Recent advances in semiconductors for photocatalytic and photoelectrochemical water splitting, *Chem. Soc. Rev.* 43 (2014) 7520–7535, <https://doi.org/10.1039/C3CS60378D>.
- [33] M. Pan, H. Zhang, G. Gao, L. Liu, W. Chen, Facet-dependent catalytic activity of nanosheet-assembled bismuth oxyiodide microspheres in degradation of bisphenol A, *Environ. Sci. Technol.* 49 (2015) 6240–6248, <https://doi.org/10.1021/acs.est.5b00626>.
- [34] J. Sun, J. Wen, G. Wu, Z. Zhang, X. Chen, G. Wang, M. Liu, Harmonizing the electronic structures on bioi with active oxygen vacancies toward facet-dependent antibacterial photodynamic therapy, *Adv. Funct. Mater.* 30 (2020), <https://doi.org/10.1002/adfm.202004108>.
- [35] R.A. Jagt, T.N. Huq, K.M. Börsig, D. Sauven, L.C. Lee, J.L. MacManus-Driscoll, R.L. Z. Hoye, Controlling the preferred orientation of layered BiOI solar absorbers, *J. Mater. Chem. C. Mater.* 8 (2020) 10791–10797, <https://doi.org/10.1039/D0TC02076A>.
- [36] C. Zhang, W. Fei, H. Wang, N. Li, D. Chen, Q. Xu, H. Li, J. He, J. Lu, p-n Heterojunction of BiOI/ZnO nanorod arrays for piezo-photocatalytic degradation of bisphenol A in water, *J. Hazard Mater.* 399 (2020), 123109, <https://doi.org/10.1016/j.jhazmat.2020.123109>.
- [37] P. Promdet, R. Quesada-Cabrera, S. Sathasivam, J. Li, A. Jiamprasertboon, J. Guo, A. Taylor, C.J. Carmalt, I.P. Parkin, High defect nanoscale ZnO films with polar facets for enhanced photocatalytic performance, *ACS Appl. Nano Mater.* 2 (2019) 2881–2889, <https://doi.org/10.1021/acsnm.9b00326>.
- [38] B.D. Vriezick, S. Patel, B.E. Davis, D.P. Birnie, Evaluation of the Tauc method for optical absorption edge determination: ZnO thin films as a model system, *Phys. Status Solidi B Basic Res* 252 (2015) 1700–1710, <https://doi.org/10.1002/pssb.201552007>.
- [39] K.S. Ahn, Y. Yan, S. Shet, T. Deutsch, J. Turner, M. Al-Jassim, Enhanced photoelectrochemical responses of ZnO films through Ga and N codoping, *Appl. Phys. Lett.* 91 (2007), <https://doi.org/10.1063/1.2822440>.
- [40] M. Li, X. Tu, Y. Wang, Y. Su, J. Hu, B. Cai, J. Lu, Z. Yang, Y. Zhang, Highly enhanced visible-light-driven photoelectrochemical performance of ZnO-modified In₂S₃ nanosheet arrays by atomic layer deposition, *Nanomicro Lett.* 10 (2018) 45, <https://doi.org/10.1007/s40820-018-0199-z>.
- [41] A. Kafizas, L. Francàs, C. Sotelo-Vazquez, M. Ling, Y. Li, E. Glover, L. McCafferty, C. Blackman, J. Darr, I. Parkin, Optimizing the activity of nanoneedle structured WO₃ photoanodes for solar water splitting: direct synthesis via chemical vapor deposition, *J. Phys. Chem. C.* 121 (2017) 5983–5993, <https://doi.org/10.1021/acs.jpcc.7b00533>.
- [42] L. Ye, L. Tian, T. Peng, L. Zan, Synthesis of highly symmetrical BiOI single-crystal nanosheets and their {001} facet-dependent photoactivity, *J. Mater. Chem.* 21 (2011) 12479–12484, <https://doi.org/10.1039/c1jm11005e>.
- [43] L. Zhang, Z. Han, W. Wang, X. Li, Y. Su, D. Jiang, X. Lei, S. Sun, Solar-light-driven pure water splitting with ultrathin BiOCl nanosheets, *Chem. A Eur. J.* 21 (2015) 18089–18094, <https://doi.org/10.1002/chem.201503778>.
- [44] A. Iqbal, A. Kafizas, C. Sotelo-Vazquez, R. Wilson, M. Ling, A. Taylor, C. Blackman, K. Bevan, I. Parkin, R. Quesada-Cabrera, Charge transport phenomena in heterojunction photocatalysts: the WO₃/TiO₂ system as an archetypal model, *ACS Appl. Mater. Interfaces* 13 (2021) 9781–9793, <https://doi.org/10.1021/acsaami.0c19692>.
- [45] A. Jiamprasertboon, A. Kafizas, M. Sachs, M. Ling, A.M. Alotaibi, Y. Lu, T. Siriratanon, I.P. Parkin, C.J. Carmalt, Heterojunction α-Fe₂O₃/ZnO films with enhanced photocatalytic properties grown by aerosol-assisted chemical vapour deposition, *Chem. A Eur. J.* 25 (2019) 11337–11345, <https://doi.org/10.1002/chem.201902175>.
- [46] B. Moss, K.K. Lim, A. Beltram, S. Moniz, J. Tang, P. Fornasiero, P. Barnes, J. Durrant, A. Kafizas, Comparing photoelectrochemical water oxidation, recombination kinetics and charge trapping in the three polymorphs of TiO₂, *Sci. Rep.* 7 (2017) 2938, <https://doi.org/10.1038/s41598-017-03065-5>.
- [47] A.H. Bhosale, S. Narra, S.S. Bhosale, E.W. Diau, Interface-enhanced charge recombination in the heterojunction between perovskite nanocrystals and BiOI nanosheets serves as an S-scheme photocatalyst for CO₂ reduction, *J. Phys. Chem. Lett.* 13 (2022) 7987–7993, <https://doi.org/10.1021/acs.jpclett.2c02153>.
- [48] S. Rieger, T. Fürmann, J.K. Stolarczyk, J. Feldmann, Optically induced coherent phonons in bismuth oxyiodide (BiOI) nanoplatelets, *Nano Lett.* 21 (2021) 7887–7893, <https://doi.org/10.1021/acs.nanolett.1c00530>.
- [49] T.N. Huq, L.C. Lee, L. Eyre, W. Li, R.A. Jagt, C. Kim, S. Fearn, V. Pecunia, F. Deschler, J.L. MacManus-Driscoll, R.L.Z. Hoye, Electronic structure and optoelectronic properties of bismuth oxyiodide robust against percent-level iodine-, oxygen-, and bismuth-related surface defects, *Adv. Funct. Mater.* 30 (2020), <https://doi.org/10.1002/adfm.201909983>.
- [50] A.M. Chang, Y.H. Chen, C.C. Lai, Y.C. Pu, Synergistic effects of surface passivation and charge separation to improve photo-electrochemical performance of BiOI nanoflakes by Au nanoparticle decoration, *ACS Appl. Mater. Interfaces* 13 (2021) 5721–5730, <https://doi.org/10.1021/acsaami.0c18430>.
- [51] K. Li, K. Gong, J. Liu, Y. Yang, I. Nabi, A.U.R. Bacha, H. Cheng, J. Han, L. Zhang, New insights into the role of sulfite in BiOX photocatalytic pollutants elimination: In-operando generation of plasmonic Bi metal and oxygen vacancies, *J. Hazard Mater.* 418 (2021), 126207, <https://doi.org/10.1016/j.jhazmat.2021.126207>.
- [52] J. Han, W. Qiu, W. Gao, Potential dissolution and photo-dissolution of ZnO thin films, *J. Hazard Mater.* 178 (2010) 115–122, <https://doi.org/10.1016/J.JHAZMAT.2010.01.050>.